Science
AAAS

Experimental Realization of a Three-Dimensional Topological Insulator, Bi 2Te3

Y. L. Chen, *et al.*

Science **325**, 178 (2009);
DOI: 10.1126/science.1173034

Experimental Realization of a Three-Dimensional Topological Insulator, Bi_2Te_3

Y. L. Chen,[1,2,3] J. G. Analytis,[1,2] J.-H. Chu,[1,2] Z. K. Liu,[1,2] S.-K. Mo,[2,3] X. L. Qi,[1,2] H. J. Zhang,[4] D. H. Lu,[1] X. Dai,[4] Z. Fang,[4] S. C. Zhang,[1,2] I. R. Fisher,[1,2] Z. Hussain,[3] Z.-X. Shen[1,2]*

Three-dimensional topological insulators are a new state of quantum matter with a bulk gap and odd number of relativistic Dirac fermions on the surface. By investigating the surface state of Bi_2Te_3 with angle-resolved photoemission spectroscopy, we demonstrate that the surface state consists of a single nondegenerate Dirac cone. Furthermore, with appropriate hole doping, the Fermi level can be tuned to intersect only the surface states, indicating a full energy gap for the bulk states. Our results establish that Bi_2Te_3 is a simple model system for the three-dimensional topological insulator with a single Dirac cone on the surface. The large bulk gap of Bi_2Te_3 also points to promising potential for high-temperature spintronics applications.

Soon after the theoretical prediction (*1*), a new state of quantum matter—the two-dimensional (2D) topological insulator displaying the quantum spin Hall (QSH) effect—was experimentally observed in HgTe quantum wells (*2*). The QSH state (*3*, *4*) has an insulating gap in the bulk and gapless states at the edge where opposite spin states counterpropagate. The two opposite spin states form a single massless Dirac fermion at the edge, and the crossing of their dispersion branches at a time-reversal invariant (TRI) point is protected by the time-reversal symmetry (*5*). The dissipationless edge state transport of the QSH state may enable low-power spintronics devices.

Two-dimensional massless Dirac fermions were experimentally discovered in graphene with two inequivalent massless Dirac points for each spin orientation, giving rise to four copies of massless Dirac fermions in total. This is consistent with the experimentally observed quantized Hall conductance $2e^2/h$ (*6*), as each Dirac fermion leads to a quantized Hall conductance $e^2/2h$ in an external magnetic field (h is Planck's constant). Graphene has an even number of massless Dirac fermions, because no TRI purely 2D free fermion system can have a single or odd number of massless Dirac fermions. However, a single Dirac fermion can occur in a 2D TRI system when it is the boundary of a 3D topological insulator (*7*–*10*), which has a bulk insulating gap and odd number of gapless Dirac cones on the surface. The electrodynamics of the topological insulator is described by an additional topological term in Maxwell's equation (*10*), and the surface state leads to striking quantum phenomena such as an image magnetic monopole induced by an electric charge (*11*) and Majorana fermions induced by the proximity effect from a superconductor (*12*–*14*).

[1]Stanford Institute for Materials and Energy Sciences, SLAC National Accelerator Laboratory, 2575 Sand Hill Road, Menlo Park, CA 94025, USA. [2]Geballe Laboratory for Advanced Materials, Departments of Physics and Applied Physics, Stanford University, Stanford, CA 94305, USA. [3]Advanced Light Source, Lawrence Berkeley National Laboratory, Berkeley, CA 94720, USA. [4]Beijing National Laboratory for Condensed Matter Physics and Institute of Physics, Chinese Academy of Sciences, Beijing 100190, China.

*To whom correspondence should be addressed. E-mail: zxshen@stanford.edu

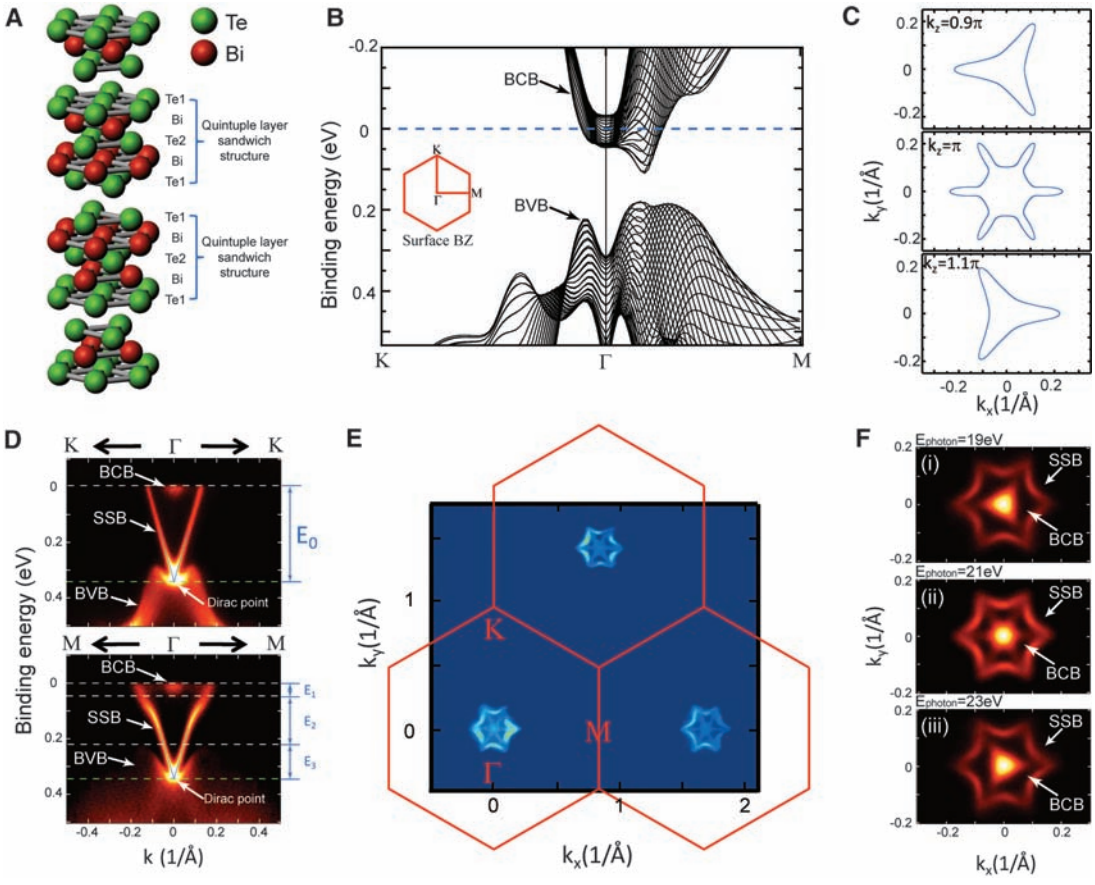

Fig. 1. Crystal and electronic structures of Bi_2Te_3. **(A)** Tetradymite-type crystal structure of Bi_2Te_3. **(B)** Calculated bulk conduction band (BCB) and bulk valance band (BVB) dispersions along high-symmetry directions of the surface BZ (see inset), with the chemical potential rigidly shifted to 45 meV above the BCB bottom at Γ to match the experimental result. **(C)** The k_z dependence of the calculated bulk FS projection on the surface BZ. **(D)** ARPES measurements of band dispersions along K-Γ-K (top) and M-Γ-M (bottom) directions. The broad bulk band (BCB and BVB) dispersions are similar to those in (B), whereas the sharp V-shape dispersion is from the surface state band (SSB). The apex of the V-shape dispersion is the Dirac point. Energy scales of the band structure are labeled as follows: E_0: binding energy of Dirac point (0.34 eV); E_1: BCB bottom binding energy (0.045 eV); E_2: bulk energy gap (0.165 eV); and E_3: energy separation between BVB top and Dirac point (0.13 eV). **(E)** Measured wide-range FS map covering three BZs, where the red hexagons represent the surface BZ. The uneven intensity of the FSs at different BZs results from the matrix element effect. **(F)** Photon energy–dependent FS maps. The shape of the inner FS changes markedly with photon energies, indicating a strong k_z dependence due to its bulk nature as predicted in (C), whereas the nonvarying shape of the outer hexagram FS confirms its surface state origin.

The 3D material HgTe under strain is predicted to have a single Dirac cone on the surface (*15*). However, experiments are difficult to perform under the strain condition. The $Bi_{1-\delta}Sb_{\delta}$ alloy is also predicted to be a 3D topological insulator in the narrow alloying content regime of $\delta = 0.07 \sim 0.22$ (*16*, *17*), and a recent angle-resolved photoemission spectroscopy (ARPES) study reveals the topological nature of the surface state despite its complexity, with as many as five branches crossing the Fermi level (E_F) (*18*).

Recently, a class of stoichiometric materials, Bi_2Te_3, Bi_2Se_3, and Sb_2Te_3, were theoretically predicted to be the simplest 3D topological insulators whose surface states consist of a single Dirac cone at the Γ point (*19*). This simplicity makes them the ideal candidates to realize the magneto-electric effect (*20*). Furthermore, the predicted large bulk gap makes them possible candidates for high-temperature spintronics applications. Independent of the theoretical proposal, an ARPES study (*21*) of Bi_2Se_3 reveals a single surface electron pocket with a Dirac point below E_F. However, a deep bulk electron pocket coexisting with the topologically nontrivial surface states was also observed in the same ARPES experiment. Therefore, the topological insulating behavior in this class of materials has yet to be established experimentally, which is the main goal of the present work.

We performed ARPES and transport experiments to investigate both the bulk and surface state electronic properties of $(Bi_{1-\delta}Sn_{\delta})_2Te_3$ crystals (where δ represents nominal Sn concentration, incorporated to compensate for the n-type doping from vacancy and anti-site defects). Further details of the sample preparation, ARPES, and transport experiments are in the supporting online material (*22*). By scanning over the entire Brillouin zone (BZ), we confirmed that the surface states consist of a single, nondegenerate Dirac cone at the Γ point. At appropriate doping (δ = 0.67%), we found that the bulk states disappear completely at E_F, thus realizing the topological insulating behavior in this class of materials. With a much larger bulk band gap (165 meV) compared to the energy scale of room temperature (26 meV), the topological protection of the surface states in this material could lead to promising applications in low-power spintronics devices at room temperature.

Figure 1 summarizes the bulk and surface electronic structures and Fermi-surface (FS) topology of undoped Bi_2Te_3. The crystal structure of Bi_2Te_3 (Fig. 1A) is of the tetradymite type, which is formed by stacking quintuple-layer groups sandwiched by three sheets of Te and two sheets of Bi within each group (*23*). Ab initio calculations predict that the undoped Bi_2Te_3 is an insulator (Fig. 1B) and that the doped FS (Fig. 1C) from the bulk conduction band projected onto the surface BZ exhibits a triangular or snowflake-like electron pocket centered at the Γ point (Fig. 1C) depending on its k_z position in reciprocal space.

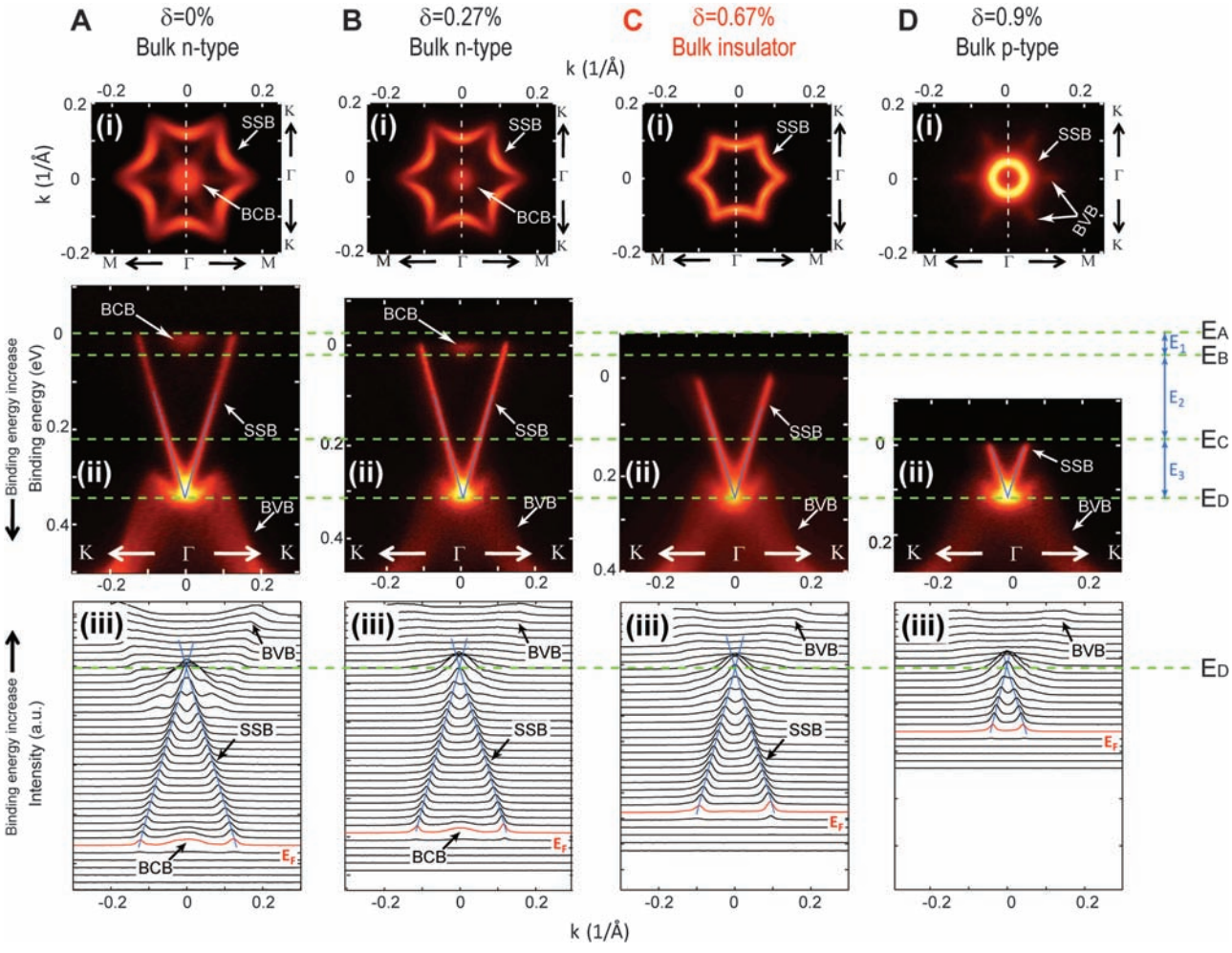

Fig. 2. Doping dependence of FSs and E_F positions. (**A** to **D**) Measured FSs and band dispersions for 0, 0.27, 0.67, and 0.9% nominally doped samples. Top row: FS topology (symmetrized according to the crystal symmetry). The FS pocket formed by SSB is observed for all dopings; its volume shrinks with increasing doping, and the shape varies from a hexagram to a hexagon from (A) to (D). The pocket from BCB also shrinks upon doping and completely vanishes in (C) and (D). In (D), six leaf-like hole pockets formed by BVB emerge outside the SSB pocket. Middle row: image plots of band dispersions along K-Γ-K direction as indicated by white dashed lines superimposed on the FSs in the top row. The E_F positions of the four doping samples are at 0.34, 0.325, 0.25, and 0.12 eV above the Dirac point, respectively. Bottom row: momentum distribution curve plots of the raw data. Definition of energy positions: E_A: E_F position of undoped Bi_2Te_3; E_B: BCB bottom; E_C: BVB top; and E_D: Dirac point position. Energy scales $E_1 \sim E_3$ are defined in Fig. 1D.

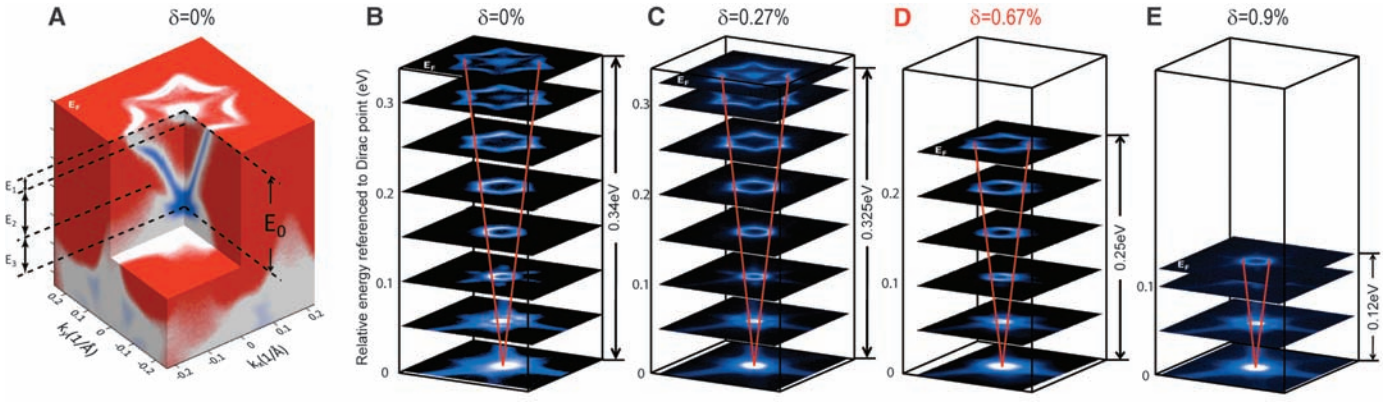

Fig. 3. (**A**) Three-dimensional illustration of the band structures of undoped Bi_2Te_3, with the characteristic energy scales $E_0 \sim E_3$ defined in Fig. 1D. (**B** to **E**) Constant-energy contours of the band structure and the evolution of the height of E_F referenced to the Dirac point for the four dopings. Red lines are guides to the eye that indicate the shape of the constant-energy band contours and intersect at the Dirac point.

Actual band dispersions measured by ARPES experiments along two high-symmetry directions are shown in Fig. 1D. In addition to the broad spectra of the bulk electron pocket on top and the "M" shape valance band at bottom, as predicted in the ab initio calculation, there is an extra sharp V-shape dispersion resulting from the surface state. The linear dispersion in both plots clearly indicates a massless Dirac fermion with a velocity of 4.05×10^5 m/s (2.67 eV·Å) and 3.87×10^5 m/s (2.55 eV·Å) along the Γ-K and Γ-M directions, respectively (*22*), which are about 40% of the value in graphene (*6*) and agree well with our first-principle calculation [by the method described in (*19*)] that yields 2.13 and 2.02 eV·Å along the Γ-K and Γ-M directions, respectively.

This sharp surface state also forms a FS pocket in addition to the calculated FSs from bulk bands. As shown in Fig. 1, E and F(ii), in each BZ there is a hexagram-shaped FS enclosing the snowflake-like bulk FS. A broad FS map covering three adjacent BZs (Fig. 1E) confirms that there is only one such hexagram FS resulting from the V-shape Dirac-type surface state in each BZ. The spin-orbit coupling (SOC) in this material is strong. The level splitting (λ) due to SOC of Bi-6p orbital is λ = 1.25 eV (*19*), about twice that in Au (λ = 0.68 eV) (*24*). Given that our energy and momentum resolution [$\delta E < 0.016$ eV and $\delta k < 0.012$(1/Å) (*22*)] is better than needed to resolve even the much smaller Au surface state splitting [$\Delta E = 0.11$ eV, $\Delta k = 0.023$(1/Å)] (*25*), the fact that we do not observe more than one set of surface state for all dopings and under all experimental conditions—including different photon energies, polarizations, and experimental setups in different synchrotrons—rules out the possibility that the Dirac cone is spin degenerate, and we encourage future spin-resolved ARPES experiments to confirm this. This observation demonstrates that Bi_2Te_3 is an ideal candidate as the parent compound for the simplest kind of 3D topological insulator (*19*)—a simplicity resembling that of the hydrogen atom in atomic physics. In contrast, graphene has two valleys with spin degeneracy, giving a total of four Dirac cones in each BZ, leading to a topological trivial state. Furthermore, because there is only one surface FS pocket in each surface BZ, the surface state will only cross E_F once between Γ and M, rather than the complex crossing of five times as observed in $Bi_{0.9}Sb_{0.1}$ (*3*, *18*).

The surface nature of the hexagram FS resulting from the sharp V-shape dispersion is further established by a photon energy dependence study (Fig. 1F). By varying the excitation photon energy, the shape of the snowflake-like bulk FS changes from a left-pointing triangle [Fig. 1F(i)] to a right-pointing triangle [Fig. 1F(iii)] as a result of the k_z dispersion of the 3D bulk electronic structure (Fig. 1C). In contrast, the shape of the hexagram-like FS does not change with the incident photon energy, confirming its 2D nature (i.e., no k_z dispersion). We note that the perfect Bi_2Te_3 single crystal is predicted to be a bulk insulator, and the electron carriers observed in our experiment arise from crystal imperfections, specifically vacancies and defects (*26*). Given the substantial bulk gap (Fig. 1D), one can tune E_F into the gap by doping holes to compensate for the electron carriers, thus realizing the topological insulator phase in this material. Because the surface state accommodates only a small number of carriers (orders of magnitude less than the bulk), the actual realization of the bulk insulating state by bulk doping is a challenging task. After experimenting with numerous doping levels by different dopants, we found Sn to be a suitable dopant and successfully doped Bi_2Te_3 into its bulk insulating phase. The effect of Sn doping is demonstrated in Fig. 2, where the FSs and band dispersions from samples of four different nominal dopings are shown from panels (A) to (D), respectively.

Taking the Dirac point position as reference, one sees the doping evolution of the FSs (Fig. 2, top row) associated with the downshift of E_F (Fig. 2, middle and bottom rows). With proper doping (Fig. 2C), the topological insulator phase of Bi_2Te_3 can be realized with the E_F residing inside the bulk gap. Unlike a simple circular Dirac cone, the observed surface state in Bi_2Te_3 exhibits richer structure. The 3D spectra intensity plot in (k_x, k_y, E) space (Fig. 3A) and the cross sections of the Dirac-like dispersion at various binding energies (Fig. 3, B to E) are demonstrated. When approaching the Dirac point from E_F, the shape of the surface state FS evolves gradually from a hexagram to a hexagon, then to a circle of shrinking volume, and finally converges into a point, the Dirac point. Comparing the shape of the bulk electron FS and the surface state FS, the hexagram shape of the surface state FS is induced by the band repulsion with the snowflake-shape bulk electron pocket. Because FSs cannot have discontinuities, the "vertices" of the hexagram and hexagon are actually smoothened. From the doping evolution of the FS topology and the band dispersions shown above, we have found convincing evidence that the 0.67% Sn-doped Bi_2Te_3 is a 3D topological insulator with a single Dirac cone and a large bulk band gap. The observations of ARPES are also supported by Hall and resistivity measurements (*22*).

The single Dirac cone of the Bi_2Te_3 family makes it the simplest model system for studying the physics of topological insulators, and the large bulk gap points to promising potential for high-temperature spintronics applications on a bulk material that is easy to produce and manipulate with current standard semiconductor technology.

References and Notes

1. B. A. Bernevig, T. L. Hughes, S.-C. Zhang, *Science* **314**, 1757 (2006).
2. M. König *et al.*, *Science* **318**, 766 (2007).
3. C. L. Kane, E. J. Mele, *Phys. Rev. Lett.* **95**, 226801 (2005).
4. B. A. Bernevig, S.-C. Zhang, *Phys. Rev. Lett.* **96**, 106802 (2006).
5. C. L. Kane, E. J. Mele, *Phys. Rev. Lett.* **95**, 146802 (2005).
6. Y. Zhang, Y.-W. Tan, H. L. Stormer, P. Kim, *Nature* **438**, 201 (2005).
7. L. Fu, C. L. Kane, E. J. Mele, *Phys. Rev. Lett.* **98**, 106803 (2007).
8. J. E. Moore, L. Balents, *Phys. Rev. B* **75**, 121306 (2007).
9. R. Roy, preprint available at http://arxiv.org/abs/cond-mat/0604211v2
10. X.-L. Qi, T. L. Hughes, S.-C. Zhang, *Phys. Rev. B* **78**, 195424 (2008).
11. X.-L. Qi, R. Li, J. Zhang, S.-C. Zhang, *Science* **323**, 1184 (2009).
12. L. Fu, C. L. Kane, *Phys. Rev. Lett.* **100**, 096407 (2008).

13. A. R. Akhmerov, J. Nilsson, C. W. J. Beenakker, *Phys. Rev. Lett.* **102**, 216404 (2009).
14. L. Fu, C. L. Kane, *Phys. Rev. Lett.* **102**, 216403 (2009).
15. X. Dai, T. L. Hughes, X.-L. Qi, Z. Fang, S.-C. Zhang, *Phys. Rev. B* **77**, 125319 (2008).
16. L. Fu, C. L. Kane, *Phys. Rev. B* **76**, 045302 (2007).
17. J. C. Y. Teo, L. Fu, C. L. Kane, *Phys. Rev. B* **78**, 045426 (2008).
18. D. Hsieh *et al.*, *Nature* **452**, 970 (2008).
19. H. Zhang *et al.*, *Nat. Phys.* **5**, 438 (2009).
20. Q. Liu, C.-X. Liu, C. Xu, X.-L. Qi, S.-C. Zhang, *Phys. Rev. Lett.* **102**, 156603 (2009).
21. Y. Xia, *et al.*, *Nat. Phys.* **5**, 398 (2009).
22. Materials and methods are available as supporting material on *Science* Online.
23. R. W. G. Wyckoff, *Crystal Structures* (Wiley, New York, 1964), vol. 2.
24. M. Vijayakumar, M. S. Gopinathan, *J. Mol. Struct.* **361**, 15 (1996).
25. S. LaShell, B. A. McDougall, E. Jensen, *Phys. Rev. Lett.* **77**, 3419 (1996).
26. C. B. Satterthwaite, R. W. Ure Jr., *Phys. Rev.* **108**, 1164 (1957).
27. We thank W. S. Lee, K. J. Lai, B. Moritz, and C. X. Liu for insightful discussions and C. Kucharczyk and L. Liu for assistance on crystal growth. This work was supported by the Department of Energy, Office of Basic Energy Sciences, under contract DE-AC02-76SF00515; H.J.Z., Z.F., and X.D. acknowledge the support by the NSF of China, the National Basic Research Program of China, and the International Science and Technology Cooperation Program of China.

Supporting Online Material
www.sciencemag.org/cgi/content/full/1173034/DC1
Materials and Methods
Figs. S1 to S4
References

4 March 2009; accepted 3 June 2009
Published online 11 June 2009;
10.1126/science.1173034
Include this information when citing this paper.

Dynamics of Chemical Bonding Mapped by Energy-Resolved 4D Electron Microscopy

Fabrizio Carbone,* Oh-Hoon Kwon, Ahmed H. Zewail†

Chemical bonding dynamics are fundamental to the understanding of properties and behavior of materials and molecules. Here, we demonstrate the potential of time-resolved, femtosecond electron energy loss spectroscopy (EELS) for mapping electronic structural changes in the course of nuclear motions. For graphite, it is found that changes of milli–electron volts in the energy range of up to 50 electron volts reveal the compression and expansion of layers on the subpicometer scale (for surface and bulk atoms). These nonequilibrium structural features are correlated with the direction of change from sp^2 [two-dimensional (2D) graphene] to sp^3 (3D-diamond) electronic hybridization, and the results are compared with theoretical charge-density calculations. The reported femtosecond time resolution of four-dimensional (4D) electron microscopy represents an advance of 10 orders of magnitude over that of conventional EELS methods.

Bonding in molecules and materials is determined by the nature of electron density distribution between the atoms. The dynamics involve the evolution of electron density in space and the motion of nuclei that occur on the attosecond and femtosecond time scale, respectively (*1*–*3*). Such changes of the charge distribution with time are responsible for the outcome of chemical reactivity and for phenomena in the condensed phase, including those of phase transitions and nanoscale quantum effects. With convergent-beam electron diffraction (*4*), the static pattern of charge-density difference maps can be visualized, and using x-ray absorption (*5*) and photoemission spectroscopy (*6*–*8*) substantial progress has been made in the study of electronic-state dynamics in bulks and on surfaces. Electron energy loss spectroscopy (EELS) is a powerful method in the study of electronic structure on the atomic scale, using aberration-corrected microscopy (*9*), and in chemical analysis of selective sites (*10*); the comparison with synchrotron-based near-edge x-ray absorption spectroscopy is impressive (*11*). The time and energy resolutions of ultrafast electron microscopy (UEM) (*12*–*16*) provide the means for the study of (combined) structural and bonding dynamics.

Here, time-resolved EELS is demonstrated in the mapping of chemical bonding dynamics, which require nearly 10 orders of magnitude increase in resolution from the detector-limited millisecond response (*17*). By following the evolution of the energy spectra (up to 50 eV) with femtosecond (fs) resolution, it was possible to resolve in graphite the dynamical changes on a millielectronvolt (subpicometer motion) scale. In this way, we examined the influence of surface and bulk atoms motion and observed correlations with electronic structural changes: contraction, expansion, and recurrences. Because the EEL spectra of a specimen in this energy range contain information about plasmonic properties of bonding carriers, their observed changes reveal the collective dynamics of valence electrons.

Graphite is an ideal test case for investigating the correlation between structural and electronic dynamics. Single-layered graphene, the first two-dimensional (2D) solid to be isolated and the strongest material known (*18*), has the orbitals on carbon as sp^2 hybrids, and in graphite the π-electron is perpendicular to the molecular plane. Strongly compressed graphite transforms into diamond, whose charge density pattern is a 3D network of covalent bonds with sp^3 hybrid orbitals. Thus, any structural perturbation on the ultrashort time scale of the motion will lead to changes in the chemical bonding and should be observable in UEM. Moreover, surface atoms have unique binding, and they too should be distinguishable in their influence from bulk atom dynamics.

The experiments were performed on a nm-thick single crystal of natural hexagonal graphite. The sample was cleaved repeatedly until a transparent film was obtained, and then deposited on a transmission electron microscopy (TEM) grid; the thickness was determined from EELS to be 108 nm. The fs-resolved EELS (or FEELS) data were recorded in our UEM, operating in the single-electron per pulse mode (*12*) to eliminate Boersch's space charge effect. A train of 220 fs infrared laser pulses (λ = 1038 nm) was split into two paths; one was frequency-doubled and used to excite the specimen with a fluence of 1.5 mJ/cm^2, and the other was frequency-tripled into the UV and directed to the photoemissive cathode to generate the electron packets. These pulses were accelerated in the TEM column and dispersed after transmission through the sample in order to provide the energy loss spectrum of the material. Details of the clocking and characterization methodology can be found in (*12*, *13*, *16*).

The experimental, static EEL spectra of graphite in our UEM, with graphene (*19*) for comparison, are displayed in Fig. 1A; Fig. 1B shows the results of theoretical calculations (*19*, *20*). The spectral feature around 7 eV is the π plasmon, the strong peak centered around 26.9 eV is the π + σ bulk plasmon, and the weaker peak on its low energy tail is due to the surface plasmon. All these features have been assigned in the literature (*19*–*21*). The agreement between the calculated EEL spectra and the experimental ones is satisfactory both for graphite and graphene. Of relevance to our studies of dynamics is the simulation of the spectra for different *c*-axis separations, ranging from twice as large as naturally occurring (2c/a; a and c are lattice constraints) to 5 times as large (*20*). This thickness dependence is displayed in Fig. 1B.

As displayed in Fig. 1, the surface and bulk plasmon bands (between 13 and 35 eV) can be

Physical Biology Center for Ultrafast Science and Technology, Arthur Amos Noyes Laboratory of Chemical Physics, California Institute of Technology, Pasadena, CA 91125, USA.

*Present address: Ecole Polytechnique Fédérale de Lausanne, CH-1015 Lausanne-Dorigny, Switzerland.
†To whom correspondence should be addressed. E-mail: zewail@caltech.edu